Ultramicroscopy 108 (2008) 1427–1431

Contents lists available at ScienceDirect

Ultramicroscopy

journal homepage: www.elsevier.com/locate/ultramic

X-ray analysis and mapping by wavelength dispersive X-ray spectroscopy in an electron microscope

Miyoko Tanaka *, Masaki Takeguchi, Kazuo Furuya

National Institute for Materials Science, 3-13 Sakura, Tsukuba, Ibaraki 305-0003, Japan

ARTICLE INFO

Keywords:
WDS
SEM
STEM
MCX
Boron compounds
W
Si
Elemental mapping

ABSTRACT

A compact and easy-to-use wavelength dispersive X-ray spectrometer using a multi-capillary X-ray lens attached to a scanning (transmission) electron microscope has been tested for thin-film analysis. B–K spectra from thin-film boron compounds (B_4C, h-BN, and B_2O_3) samples showed prominent peak shifts and detailed structural differences. Mapping images of a thin W/Si double-layer sample resolved each element clearly. Additionally, a thin SiO_2 film grown on a Si substrate was imaged with O–K X-rays. Energy and spatial resolution of the system is also discussed.

© 2008 Elsevier B.V. All rights reserved.

1. Introduction

X-ray spectroscopy performed with electron microscopes is becoming more and more important as a tool to provide complete micron- or nano-scale quantitative chemical information. The most widely adopted X-ray spectroscopy method is energy dispersive X-ray spectroscopy (EDS) using semiconductor detectors, due to its compactness, high detection efficiency, and ease of operation [1,2]. Meanwhile, wavelength dispersive X-ray spectroscopy (WDS) surpasses EDS at high-energy resolution, for its detection limits and its ability to detect light elements [3,4]. WDS is usually installed in electron probe micro analyzers (EPMAs), not in scanning electron microscopes (SEMs) or in transmission electron microscopes (TEMs). In this type of spectrometer, the curved analyzing crystal and detector are required to move along the Rowland circle; thus there are many movable parts that generate vibration and noise. Additionally, the vacuum deterioration needs to be also considered. Also, sample alignment requires micrometer-order height adjustments, which makes this type of spectrometer difficult to use as a microscope accessory.

Other types of X-ray spectroscopy are being investigated to achieve better performance. EDS by microcalorimetry using transition edge sensors is one solution. It provides about 10 times better energy resolution than traditional EDS while covering a relatively wide energy range at one time, typically around 2 keV when in a wide photon energy range configuration [5,6]. Other manufacturers aim for higher-energy resolution (−0.2 eV) and light element detection down to Li or B using varied-line-spacing gratings and back-illumination CCD detectors for EPMA [7] and TEM [8]. These methods are, however, rather for special laboratory use than for ordinary use since the instruments are very complicated and either too large or too expensive, or both.

Recent development in parallel beam X-ray spectrometers using multi-capillary X-ray (MCX) optics to collimate divergent X-rays has made it possible to perform WDS readily and easily in electron microscopes [9]. Since parallel beam spectrometers use flat crystals and simple θ–2θ scanning systems instead of curved crystals and Rowland circle mountings, they are compact and generate less vibration and noise. These characteristics make parallel beam spectrometers suitable for use in SEMs or in TEMs for materials analysis, which has been difficult to perform with EDS. Using a MCX–WDS system (SHIMADZU) attached to a SEM (JEM-7000F, JEOL), we achieved light element analysis down to B for both bulk and TEM thin-film samples with high-energy resolution [10].

In the present study, we modified this SEM–WDS system to a scanning transmission electron microscopy (STEM) compatible system and carried out light element analysis such as B, C, N, and O as well as elemental mapping. Thin-film TEM specimens were analyzed, as well as bulk specimens. A set of boron compounds (h-BN, B_2O_3, and B_4C), α-Al_2O_3, W/Si double layer specimen, and a SiO_2 film grown on a Si substrate were analyzed.

2. Instrumentation

The MCX–WDS system is attached to the column of the JEM-7000F SEM. The microscope chamber is specially modified with

* Corresponding author.
E-mail address: TANAKA.Miyoko@nims.go.jp (M. Tanaka).

0304-3991/$ - see front matter © 2008 Elsevier B.V. All rights reserved.
doi:10.1016/j.ultramic.2008.05.011

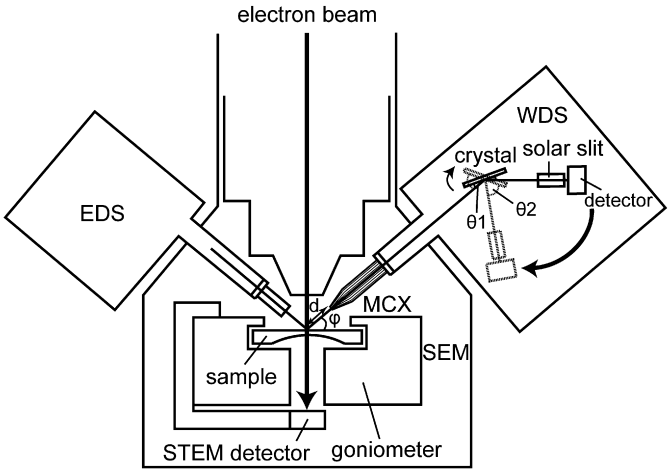

Fig. 1. A schematic drawing of the SEM–WDS system. The working distance was set at $d = 22.5$ mm, with a detection angle of $\varphi = 40^\circ$. The SEM detector, a FIB and an ion gun module are not shown for clarity.

six ports viewing samples at angles between 35° and 45°. The ports are presently equipped with a secondary electron detector (SED), a focused ion beam (FIB) module (SM-Z05032T, JEOL), a duoplasmatron ion beam module (IOG-30G, Ionoptica), an EDS module (JED-2200, JEOL), and the MCX–WDS. The take-off angle and working distance of the MCX–WDS are set up at 40° and 22.5 mm, respectively, to achieve maximum capture efficiency, as illustrated in Fig. 1. The SED and ion beam modules are not shown in the figure for clarity. A turbo molecular pump is adopted to achieve dry pumping.

The MCX–WDS system is composed of a MCX, a set of analyzing flat crystals which can be exchanged by a motor-drive system, a soller slit, and a gas flow proportional counter using PR gas (Ar:CH_4 = 9:1). The analyzing crystals and the counter move to keep a θ–2θ positional relationship. The latter collects only those X-rays that satisfy the Bragg condition. Since the crystals and the detector do not need to move along the Rowland circle, the system is compact ($230 \times 230 \times 110\,mm^3$) and generates less vibration or noise. Also, focusing the analyzer is not as restrictive as for EPMAs due to the collection efficiency of the MCX lens. The system has four analyzing flat crystals, LiF, ADP, RAP, and PbST, whose plane spacings are 0.201, 0.532, 1.306, and 5.01 nm, respectively. It covers the energy range from 135 eV to 10 keV with the capability of detecting B to U. Compared with traditional EPMAs where analysis points are restricted to within several μm height and width, the size of the sweet spot of the present MCX–WDS is much wider, approximately 0.2 mm in height and 0.4 mm in both width and depth.

The MCX–WDS software provides both spectra and mapping images. Mapping images are to be acquired as 32×32 to 1024×1024 pixel sizes with any dwell time.

STEM is a functional capability of SEM. A bright field (BF) detector (PN junction type) is set on the backside of the goniometer specimen stage. Thus, it is possible to observe and analyze both bulk and TEM thin film samples with this system.

3. Basic performance results and discussion

For most experiments, primary electron energy of 15 keV was used at about 200 nA current. Measurement time varied depending on the experiments. A pulse height analyzer was not used in this instance as the target peaks become too weak for most cases. SEM and STEM images were acquired at 15 and 30 kV, respectively.

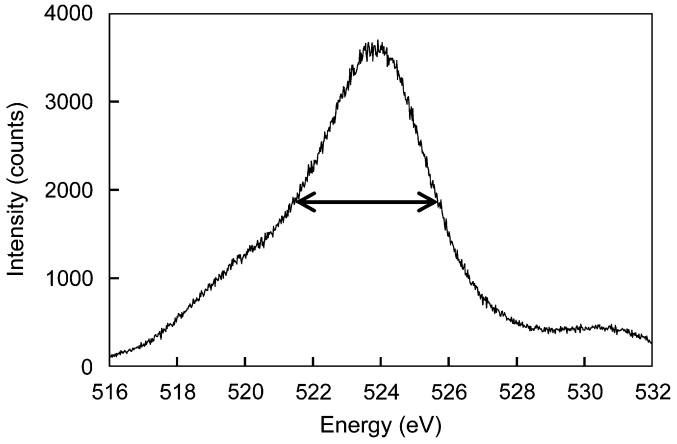

Fig. 2. O–K X-ray spectrum of an Al_2O_3 bulk sample. The FWHM is measured to be 4.3 eV.

3.1. Energy resolution and minimum detection limit

High-energy resolution, high sensitivity, and detection of light elements are the main strong points of WDS analysis. Firstly, energy resolution was measured for a bulk α-Al_2O_3 sample. Fig. 2 shows O–K peaks analyzed with RAP crystals for 7500 s. The full-width at half-maximum (FWHM) was measured at 4.3 eV. This value is comparable to the levels obtained with those of curved crystal analyzers. Minimum detection limit (MDL), is defined as [11]

$$MDL = C \times \sqrt{N}/S$$

where C is the concentration of the object elements in weight, S is the signal intensity from the object element, and N is the summation of background, tails of peaks of other elements, system noise, natural radiation, etc., and was calculated from the spectrum in Fig. 2 as 570 ppm. This value is somewhat worse than those obtained from EPMA because the present system has probe current limitations directly affecting the X-ray intensity and hence the SN ratio.

3.2. Analysis of B compounds

Light element analysis is difficult because of low fluorescent yields [12] and low sensitivity [11]. The fluorescent yield for B–K is, for example, 4.3×10^{-4}, according to Laberrigue-Frolow and Radvanyi [11]. The ionization cross section, which also determines the total X-ray intensity, is much lower than those of heavier atoms due to the low K-shell excitation energy and hence very high overvoltage ratio [13,14]. Low-energy X-rays are easily absorbed, as well. However, light element analysis gives much useful information. The distribution of light elements sometimes determines product performance. Also, it gives information on the bonding condition directly through peak energy and peak shape [15,16]. Here, K-line analysis of B compounds was performed to confirm the system detection efficiency.

Three types of B compounds, h-BN, B_4C, and B_2O_3, were analyzed. Their respective spectra are shown in Fig. 3. In all spectra, the PbST crystal was used within a measurement time of 4.3 h. All samples were TEM thin specimens. The h-BN substrate was cut and mechanically polished for thin-film preparation, while the B_4C and B_2O_3 specimens were prepared by the powder technique.

The K-line emission spectra from the three boron compounds are shown in Fig. 3. The spectra are normalized to unity here. As can be seen, the B_4C spectrum consisted of only one band, which

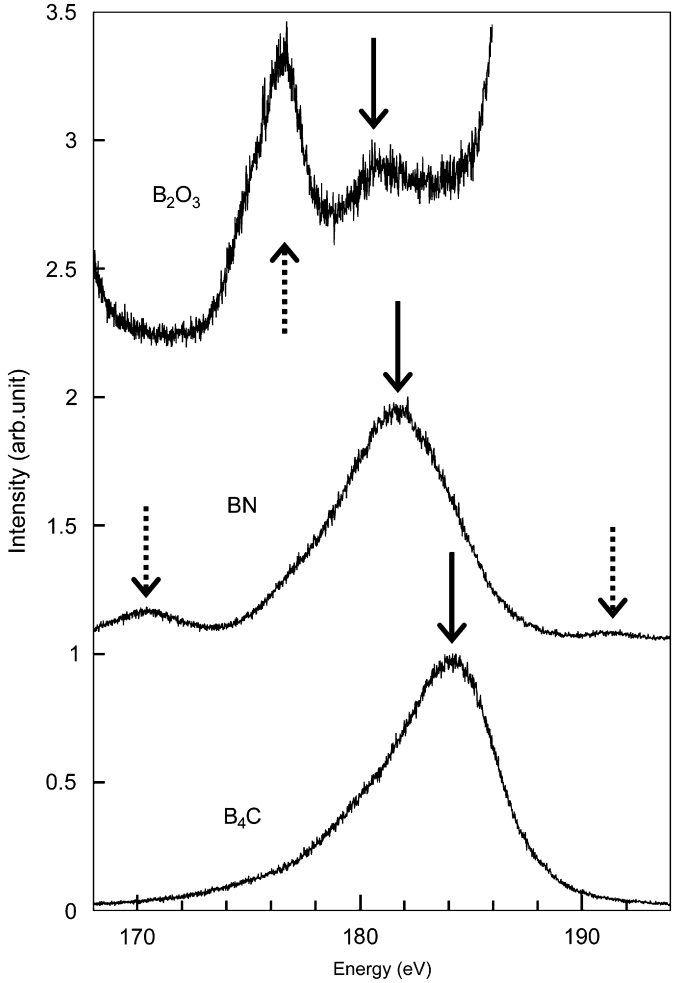

Fig. 3. B–K X-ray diffraction spectra of a B_4C, h-BN, and B_2O_3 TEM samples. Except for the prominent chemical shifts, the detailed structure of the peaks differs from one another, representing their bonding states.

is rather asymmetrical in shape. The peak is located at about 184.2 eV. In the case of h-BN, the main band is quite symmetrical in shape and has shifted to a lower energy, approximately 181.8 eV. Low- and high-energy satellite peaks appear as indicated by dashed arrows. The same tendency should have been observed with the B_2O_3 sample, but the intensity was very weak and only the main band at about 180.5 eV was detected, as shown in the figure. In contrast, the third-order reflection from the O–K peak appears distinctly at around 176.5 eV as indicated by a dashed arrow. There are two large peaks located in the high- and low-energy area as a result of a Cu grid and a sample holder; therefore, the satellite peaks could not be differentiated.

The crystal structure of B_4C is composed of $B_{11}C$ icosahedra clusters directly linked by covalent bonds and indirectly linked by C–B–C chains along the main diagonal [17,18]. In the measured emission spectrum, the main emission peak is due to a B2p–B1s transition. When B–C chemical bonds are formed, the local electron density from the B atom p-level decreases. At the same time the local electron density for B–B bonds does not change. This leads to a shift of the boron valence band towards higher energies and to a decrease of the B2p–B1s transition energy. The band appears as asymmetric because the band represents both B–C and B–B bonding states.

The h-BN has a graphite-like structure, and in its modifications the B and N atoms form σ-bonds with each other. Also, π-bonding occurs in the layer planes due to interactions of B atoms vacant atomic orbitals with the lone electron pair of the N atoms. Bonding between the layers in the h-BN structure is also largely determined by the van der Waals and electrostatic interactions as a result of oppositely charged boron and nitrogen atoms in layers located one above another [19]. The main band is thus an overlap of π and σ valence states. On the other hand, B_2O_3 has a hexagonal structure in which B atoms form sp_2-planar bonding in $B–O_3$ triangular units. These triangles make infinite interconnected chains such that each O atom has four O neighbors [20]. In both cases, the main spectral peaks correspond to B2p–B1s transitions. The B–K edge chemical shift correlates with the electronegativity of the ligand. The B–K edge shifts to a higher energy with an associated increase in electronegativity of the ligand from C to O as shown in the figure. The low-energy satellite peak observed for h-BN can be attributed to a transition from a molecular orbital consisting of B2p and NO2s character to a B1s core hole. The weak high-energy peaks are associated with the core excitonic emission [21,22].

The present results suggest that the MCX–WDS system is sufficient in detecting not only chemical shifts but also detailed chemical information from thin-film samples.

3.3. WDS mapping of thin film sample

Elemental mapping is one of the principal advantages of X-ray analysis as it provides clear and direct information regarding the distribution and quantity of each element in the sample. Comparing the map with a SEM or a STEM image will provide a correlation between morphology and composition. The only disadvantage of mapping would be a long acquisition time if good energy resolution is required. For instance, a 64×64 pixel image with a dwell time of 0.5 s requires an acquisition time of about 2000 s for only one image frame. Usually, multiple frames and/or larger pixel images are necessary to smooth X-ray intensities and to achieve better spatial resolution. Alternatively, we can use shorter dwell times at the sacrifice of intensities. In that case, 128×128 or larger pixel images could be obtained within a comparable acquisition time. MCX high detection efficiencies are beneficial to the effective collection of X-rays and to shorten the acquisition time, in this regard.

The number of X-rays emitted from the specimen is roughly proportional to the sample thickness when the thickness is less than an escape depth (−1 μm) [23]. Because a typical TEM sample thickness ranges from 10 to 20 nm, the X-ray intensity from thin-film specimens is about 10^{-3}–10^{-2} times lower than from bulk specimens. Elemental mapping for thin film samples by WDS is thus challenging and appropriate to test the efficiency of our system. A thin W film was attached to a Si substrate for cross-sectional analysis. For gluing, GATAN two-component epoxy glue is used. The sample was cut, mechanically polished, pasted on a grid and finally thinned by a 30 kV Ga-FIB.

Fig. 4 shows SEM and STEM images and elemental maps of the W/Si double-layer specimen pasted on an Au thin foil. The central part of the image (inside a dotted line) is the FIB milled area. The upper Si area appears thinner (Fig. 4a) than the lower W area representing the difference in sputtering rate by Ga ions [24]. In the magnified STEM BF image (Fig. 4b), the thin areas are well resolved. Elemental maps in Fig. 4(c)–(e) correspond to a W–Mα (1,775 eV), a Si–Kα (1,740 eV) and an Au–Mα (2,123 eV) image, all taken with the ADP crystal. Fig. 4(f) is a montage image. These maps are taken with the same magnification as Fig. 4(a). The mapping images were taken at 64×64 pixels per frame with a dwell time of 0.5 s with the frames integrated five times. Therefore, the total acquisition time was calculated to be about 2.8 h. The maps appear in the ratio of 5:4 due to the scanning rate

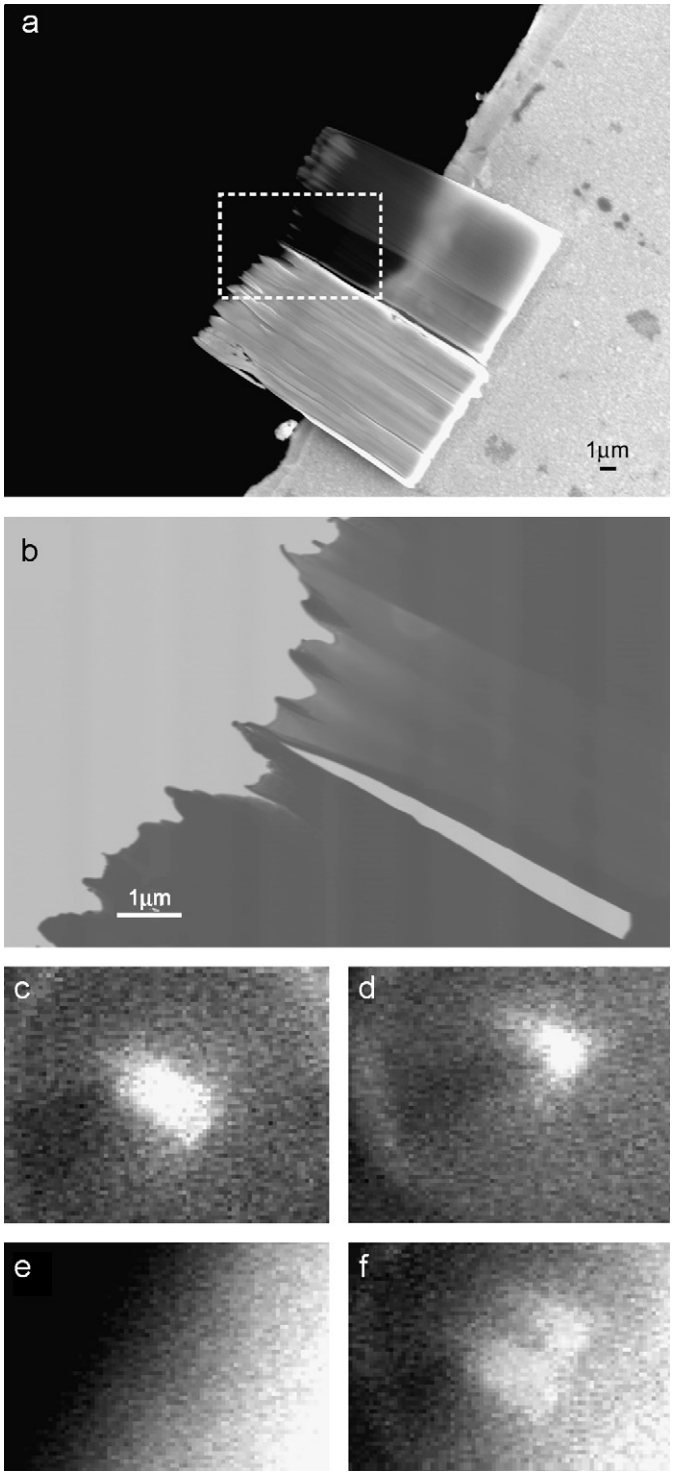

Fig. 4. Microscopic images and elemental maps of a W/Si double layer TEM sample. (a) The sample SEM image and (b) the enlarged STEM image. The upper layer corresponds to the Si area, while the lower layer corresponds to the W area. The sample is glued on an Au foil. Elemental maps of (c) W, (d) Si, and (e) Au, and (f) a montage map.

differences between horizontal and vertical lines. As seen in the figures, W and Si layers are well resolved. It is noted that both the bulk part of the films pasted on the Au foil and the thin film part, which protrudes into the vacuum, emitted X-rays and contributed to the imaging. Even the Si thin film part has some intensity. In Fig. 4(c) and (d), ring-like contrasts which appear to surround each thin film are observed. The radius of this ring is about 10 μm. This effect can be attributed to the edge effect, where the X-ray intensity first decreases due to the decrease in the production area, then increases due to the decrease in absorption [11]. Thus the mapping images were gained successfully due to the high-energy resolution of the WDS system and collection efficiency of the MCX lens.

3.4. WDS mapping at an interface

WDS spatial resolution analysis is mainly determined by (1) beam size, (2) electron penetration depth in targets [25], (3) X-ray production function including absorption [26], and (4) sample geometry. Sample geometry becomes especially critical when treating thin films, polycrystalline materials, particles on supports, and samples with edges as described in Section 3.3. The fluorescent excitation effect is another factor that may affect spatial resolution [11]. Additionally, the spatial resolution of mapping requires other factors. X-ray intensities from each grain or particle should be as high as 1000 cps to effectively distinguish in a mapping image [11]. The pixel size and the mapping area size should be carefully selected as well.

In the present study, elemental maps of a thermally grown silicon oxide film on a silicon substrate (bulk sample) were

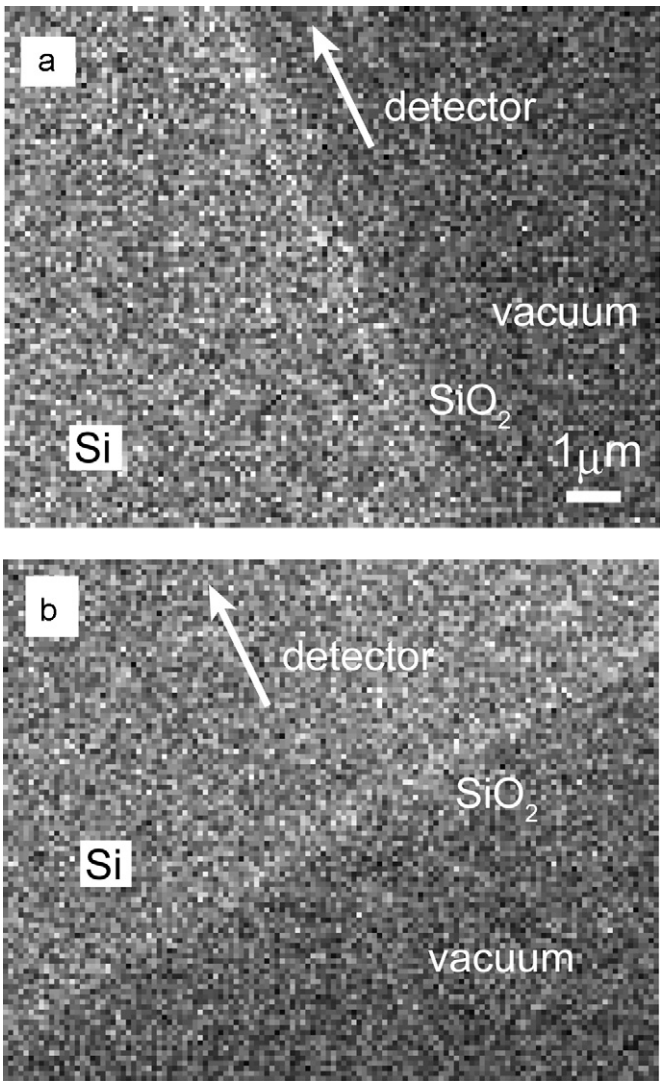

Fig. 5. O–K X-ray maps of a thermally grown SiO_2 layer on a Si substrate taken (a) parallel and (b) perpendicular and facing towards the back of the detector.

acquired to evaluate the map's effective spatial resolutions. The thickness of the film is about 100 nm. The O–K maps, taken at two different sample orientations, are shown in Fig. 5. The X-ray detector is placed in the upper left direction. The sample was set in parallel (Fig. 5a) and perpendicular and facing toward the back (Fig. 5b) position in order to discriminate the edge effect. The mapping images were taken with a PbST crystal at 128×128 pixels per frame, a dwell time of 0.5 s with frames integrated eight times. Therefore, the total acquisition time is about 18 h. In both images, the SiO_2 film appears as a bright line in the center.

Under the present experimental conditions, the effective production depth of O–K X-rays was about 1.23 μm [11,25]. However, because low-energy (0.525 keV) O–K X-rays are very easily absorbed in the matrix, the O–K area would appear smaller than this value. Using the Lambert–Beer low

$$I = I_0 \exp(-\kappa\rho x)$$

where I_0 and I are intensity before and after absorption, respectively, and κ is mass absorption coefficient, ρ is density of the matrix, and x is the distance from the electron beam incident site, I becomes $0.8I_0$ when $x = 0.1$ μm, and $0.5I_0$ when $x = 0.3$ μm. Here, mass absorption coefficient of Si for 0.525 keV X-ray is about 10^4 [27]; the beam size for 15 keV electrons at 200 nA is about 0.1 μm, and the fluorescent excitation effect is negligible. Thus a line of 0.1 μm SiO_2 would appear as

$$2(x \text{ of a certain absorption}) + (\text{beam size}),$$

which is in the range of 0.3–0.7 μm. Because the image size of the maps is $12\,\mu m \times 9.6\,\mu m$, the SiO_2 line would then appear as a width equivalent to 3–8 pixels. It does appear as about a 5-pixel width line in both images. The intensity ratio between the line and the background looks higher in Fig. 5(a) than in Fig. 5(b) probably due to the edge effect. Because the vacuum side, where no absorption is expected, is facing towards the back of the X-ray detector, the image in Fig. 5(b) should be affected minimally by this effect.

The film thickness was comparable to the beam size in the present case. Even if it were thinner, it would still appear to be almost the same size line as the effective production depth is much larger than the film thickness. If the sample is thinner, the production area would be smaller and the X-ray intensities would not be high enough to be distinguished from the background as described in Section 3.3. Heavier atoms of higher excitation energies would have a smaller production area and less absorption. In those specific cases, the spatial resolution would be different.

4. Conclusion

We have carried out several basic analyses to test the capability of the MCX–WDS system attached to the SEM/STEM. The system uses a flat analyzing crystal and simple θ–2θ scanning system with a multicapillary lens efficiently collecting emitted X-rays from samples. The system possesses four analyzing crystals that can be easily exchanged and cover the energy range from 135 eV to 10 keV. From the spectrum of a bulk α-Al_2O_3 sample, the energy resolution and minimum detection limit were measured to be 4.3 eV and 570 ppm, respectively. Analysis of thin-film B compounds (B_4C, h-BN, and B_2O_3) revealed their chemical shifts and detailed chemical information. WDS mapping of a W/Si double-layer sample was successful for a TEM specimen. An elemental map of a thin SiO_2 film grown on a Si substrate was also acquired as a bulk specimen. These basic results suggest that the present SEM–WDS system has enough functionality to analyze light elements for both bulk and thin film specimens with high resolution.

Acknowledgments

The authors would like to thank Dr. Hiroyoshi Soezima (Shimadzu Scientific Research) for much useful advice and discussions. This study has been supported by the Japan Science and Technology Agency, and the Nuclear Research Funds of The Ministry of Education, Culture, Sports, Science and Technology of the Japanese Government.

References

[1] J.L. Friel, E. Lyman, Microsc. Microanal. 12 (2006) 2.
[2] U. Alber, H. Müllejans, M. Rühle, Ultramicroscopy 69 (1997) 105.
[3] C.-U. Ro, K.-Y. Oh, J. Osán, J. de Hoog, A. Worobiec, R. Van Grieken, Anal. Chem. 73 (2001) 4574.
[4] Y. Osada, J. Mater. Sci. 38 (2003) 1457.
[5] D.E. Newbury, Microsc. Microanal. 12 (2006) 527.
[6] K. Tanaka, A. Odawara, A. Nagata, M. Ikeda, Y. Baba, S. Nakayama, Surf. Interf. Anal. 38 (2006) 1646.
[7] S. Fukushima, T. Kimura, T. Ogiwara, K. Tsukamoto, T. Tazawa, S. Tanuma, Microsc. Microanal. 12 (Supp. 2) (2006) 871.
[8] M. Terauchi, M. Kawana, Ultramicroscopy 106 (2006) 1069.
[9] H. Soejima, T. Kitamura, T. Marui, K. Furuya, Proc. IMC16 2 (2006) 872.
[10] M. Tanaka, M. Takeguchi, K. Furuy, A.H. Soejima, T. Kitamura, T. Marui, M. Kawai, K. Miyazaki, Proc. NIMS Conf. 77 (2007).
[11] P. Laberrigue-Frolow, P. Radvanyi, J. Phys. Radiat. 17 (1956) 944.
[12] H. Soezima, Electron Probe Microanalysis, Nikkann Kogyo Shimbun, Tokyo, 1987.
[13] E. Casnati, A. Tartati, C. Baraldi, J. Phys. B 15 (1982) 155.
[14] C.S. Campos, M.A.Z. Vasconcellos, J.C. Trincavelli, S. Segui, J. Phys. B 40 (2007) 3835.
[15] C.-U. Ro, J. Osán, R. Van Grieken, Anal. Chem. 71 (1999) 1521.
[16] T. Wenzel, K.G. Nickel, J. Glaser, H.J. Meyer, D. Eyidi, O. Eibl, Phys. Stat. Sol. A 198 (2003) 374.
[17] E.R. Tallant, T.L. Aselage, A.N. Champbell, E. Emin, Phys. Rev. B 40 (1989) 5649.
[18] D. Li, W.Y. Ching, Phys. Rev. B 52 (1995) 17073.
[19] R.S. Pease, Acta Crystallogr 5 (1952) 356.
[20] G.E. Gurr, P.W. Montgomery, C.D. Knutson, B.T. Gorres, Acta Crystallogr B26 (1970) 906.
[21] W.L. O'Brien, J. Jia, Q.-Y. Dong, T.A. Callcott, K.E. Miyano, D.L. Ederer, D.R. Mueller, C.-C. Kao, Phys. Rev. Lett. 70 (1993) 238.
[22] Y. Muramatsu, M. Oshima, H. Kato, Phys. Rev. Lett. 71 (1993) 448.
[23] R. Castaing, Advances in Electronics and Electron Physics, Vol. 13, Academic Press, 1960, p. 317.
[24] X. Xu, A.D. Della Ratta, J. Sosonkin, J. Melngalis, J. Vac. Sci. Technol. B 10 (1992) 2675.
[25] K. Kanaya, S. Oakayama, J. Phys. D 5 (1972) 43.
[26] D.B. Brown, D.B. Wittry, D.F. Kyser, J. Appl. Phys. 40 (1969) 1627.
[27] J. Janesick, T. Elliott, F. Pool, IEEE Trans. Nucl. Sci. 36 (1989) 572.